JOURNAL OF THERMOPHYSICS AND HEAT TRANSFER
Vol. 16, No. 2, April–June 2002

Transonic Film Cooling Effectiveness from Shaped Holes on a Simulated Turbine Airfoil

Tetsuji Furukawa* and Phillip M. Ligrani†
University of Utah, Salt Lake City, Utah 84112-9208

The performance of film cooling on a simulated transonic, turbine airfoil is investigated using an experimental apparatus designed especially for this purpose. A symmetric airfoil with the same transonic Mach number distribution on both sides is employed. Mach numbers along the airfoil surface range from 0.4 to 1.24 and match values on the suction surface of airfoils from operating aeroengines. Film cooling holes are located on one side of the airfoil near the passage throat where the freestream Mach number is nominally 1.07. Three different film cooling configurations are investigated with density ratios of about 1.4–1.6 over a range of blowing ratios, momentum flux ratios, and pressure ratios. These include single rows of 1) cylindrical holes with simple angle orientations, 2) laid-back-fan-shaped holes with simple angle orientations, and 3) laid-back-fan-shaped holes with compound angle orientations. New spatially resolved and spatially averaged effectiveness data and discharge coefficients are provided for these hole geometries with airfoil suction surface geometry, flow conditions, and boundary-layer development that simulate engine operating conditions. The highest local and spatially averaged film cooling effectiveness magnitudes are generally obtained with laid-back-fan-shaped holes oriented with compound angles, followed by laid-back-fan-shaped holes oriented with simple angles, which are then followed by round, cylindrical holes oriented with simple angle orientations.

Nomenclature

A	=	area
C_D	=	discharge coefficient
c	=	airfoil chord length
d	=	diameter of the film cooling hole entrances
I	=	momentum flux ratio, $\rho_c U_c^2/\rho_m U_m^2$
k	=	ratio of specific heats
M	=	Mach number
m	=	blowing ratio, $\rho_c U_c/\rho_m U_m$
$\dot{m}$	=	mass flow rate
p	=	pressure
R	=	gas constant
T	=	temperature
U	=	time- and spatially averaged velocity
x	=	streamwise coordinate measured from downstream edge of film cooling holes
z	=	spanwise coordinate measured from spanwise centerline of center film cooling hole
η	=	local adiabatic film cooling effectiveness, $(T_{\text{aw}} - T_{rm})/(T_{tc} - T_{rm})$
$\bar{\eta}$	=	spanwise-averaged adiabatic film cooling effectiveness
ρ	=	density

Subscripts

aw	=	adiabatic wall value
c	=	injectant or film coolant value at exit planes of film cooling holes
ideal	=	ideal isentropic value
m	=	local freestream value
r	=	recovery value
t	=	total or stagnation value

Received 16 April 2001; revision received 15 August 2001; accepted for publication 16 October 2001.

*Graduate Student, Convective Heat Transfer Laboratory, Department of Mechanical Engineering, 50 S. Central Campus Drive, MEB 2202.

†Professor, Convective Heat Transfer Laboratory, Department of Mechanical Engineering, 50 S. Central Campus Drive, MEB 2202; ligrani@mech.utah.edu.

I. Introduction

In recent years, researchers, manufacturers, and designers have devoted increased attention to the thermal performance of shaped film cooling holes on turbine airfoils in gas turbine engines. This is because these holes often provide higher levels of thermal protection compared to round, cylindrical shaped holes. Investigations of the thermal performance of shaped holes consider a variety of film hole geometries, including conical-diffused holes,[1,2] diffused-trapezoidal shaped holes,[3] square holes,[4] shaped-inclined slots,[5] forward-diffused holes,[6–14] laterally diffused (or fan-shaped) holes,[7–9,11,14–19] and forward laterally diffused (or laid-back-fan-shaped) holes.[12,15–23] A number of these studies consider shaped holes oriented with compound angle orientations.[2,6,9,10,14,18,22] Only four consider shaped film hole geometries with simulated turbine airfoil geometry[18,19,23] or high Mach number flow conditions along a flat plate.[17]

Of these investigations, Reiss and Bolcs[18] investigate cylinder, leading-edge film cooling from fan-shaped holes and laid-back-fan-shaped holes with compound angle orientations. Teng and Han[19] and Brandt et al.[23] consider film cooling on turbine airfoil suction surfaces with laid-back-fan-shaped holes with simple angle orientations. Only the experimental study by Gritsch et al.[17] is conducted with high subsonic and supersonic Mach numbers that approximate the conditions that exist in operating engines with transonic turbine components. Mainstream Mach numbers are 0.3, 0.6, and 1.2, and coolant passage Mach numbers are 0 and 0.6. Three different types of single holes are employed, each with a simple angle orientation. Constant pressure gradients are used in the freestream flow along the flat plate test section. With this arrangement, higher effectiveness values are generally produced by holes with laid-back-fan shapes (and simple angle orientations) than by cylindrical holes and fan-shaped holes (both also with simple angle orientations).

The present study employs a test section especially designed for measurements of local and spatially averaged adiabatic film cooling effectiveness distributions and discharge coefficients from film cooling holes located on the simulated suction surface of a turbine airfoil. A symmetric airfoil is employed with the same transonic

Mach number distribution on both sides. Mach numbers along the airfoil surface range from 0.4 to 1.24 and match values on the suction surfaces of airfoils from operating aeroengines. Film cooling holes are located on one side of the airfoil near the passage throat where the freestream Mach number is nominally 1.07. Three different film cooling configurations are investigated with density ratios of about 1.4–1.6 over a range of blowing ratios, momentum flux ratios, Mach number ratios, and pressure ratios. In each case, a single row of holes is employed. Thus, new suction surface film cooling effectiveness data and discharge coefficients are provided beyond that provided by earlier investigators. In particular, the present study is the first one to investigate the performance of rows of laid-back-fan-shaped holes, with and without compound angle orientations, with airfoil suction surface geometry, flow conditions, freestream pressure gradient, and boundary-layer development that simulate transonic engine operating conditions.

The only other existing experimental study of similarly shaped holes at high Mach numbers utilizes a single hole (with a simple angle orientation) in a near-zero pressure gradient.[17] The two other related studies, which employ turbine airfoils, both utilize laid-back-fan-shaped holes with simple angle orientations, and either low-speed, incompressible flows[19] or low subsonic Mach numbers.[23] Thus, the experimental data in the present paper are new and different from results presented elsewhere, because data are given downstream of a row of laid-back-fan-shaped holes with simple angle orientations and a row of laid-back-fan-shaped holes with compound angle orientations. Film cooling data at transonic flow conditions are important because data at subsonic conditions cannot be used to simulate physical phenomena, such as shock waves. This makes the data from the present paper unique and valuable for the design of gas turbine blade components, as well as for the further development of more widely applicable numerical models and prediction schemes.

II. Test Section and Film Cooling Hole Geometries

A schematic diagram of the nonturning airfoil cascade test section is shown in Fig. 1a. The test section is made up of two acrylic side walls and top and bottom walls made of steel and acrylic. The two side walls are flat, whereas the top and bottom walls are contoured to form a converging–diverging shape that produces the desired Mach number distribution along the symmetric test airfoil. Because significant flow turning is not included, the camber curvature, present in many cascades with multiple airfoils, is not present.

A schematic diagram of the cross section of one symmetric airfoil tested is shown in Fig. 1b. This is constructed especially for this study using electrodischarge machining (EDM) and other precision machining techniques. The airfoil chord length c is 7.62 cm. The effective pitch is 5.08 cm. This pitch value is based on the locations of the top and bottom walls relative to the airfoil and the fact that each induces a static pressure variation along its length, which is similar to that midway between two adjacent blades.[24] Lexan (or polycarbonate) inserts are used to produce a test surface with low conductivity (0.188 W/mK), which models an adiabatic surface. Note that the film cooling holes are also contained in these inserts to provide a continuous test surface for surface temperature measurements. The trailing edge of the symmetric airfoil is a 1.14-mm-radius round semicircle, designed to produce the wake flows of turbine airfoils employed in operating engines. The symmetric airfoil shape is employed to provide sufficient interior space for a plenum for film cooling injection, while maintaining appropriately scaled injection hole diameter and trailing-edge thickness. Note that the convex curvature of the airfoil (relative to the camber line) is an exact match to that employed for suction surfaces in an operating transonic turbine. Geometric dimensions of the contoured test walls and airfoil are given by Jackson et al.[24]

Figure 1b also shows that a step is included along the plenum wall in the plenum just upstream of the film cooling hole entrances. This step acts 1) to direct flow from the plenum so that it is perpendicular to the streamwise (or bulk flow) direction at the entrances to the film cooling holes and 2) to spread the cross flow uniformly over the entrances of all of the film holes. This perpendicular film injectant

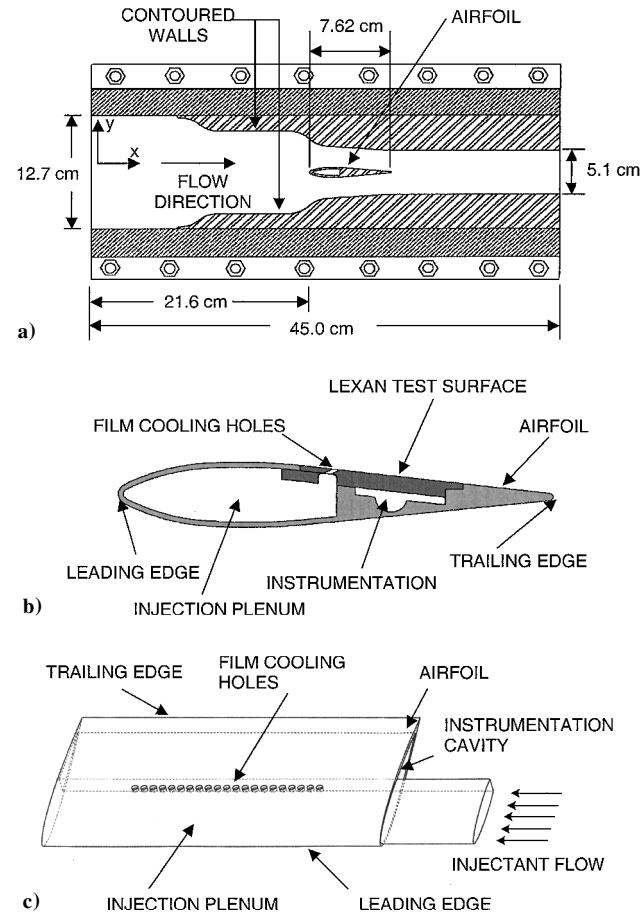

Fig. 1 Schematic diagrams: a) test section; b) test airfoil, cut-away side view; and c) test airfoil, three-dimensional view.

(with Mach numbers from 0.2 to 0.5 at the entrances of the holes) is employed to create an injectant inlet flow condition, which is similar to that which exists in many operating transonic turbines. Figure 1c then shows the overall airfoil plenum arrangement.

The geometric characteristics of the three hole configurations studied are shown in Figs. 2a–2c. In this and other figures, the following acronyms are used for cylindrical simple-angle holes (CYSA), laid-back-fan-shaped holes with simple angle orientations (LBFS-SA), and laid-back-fan-shaped holes with compound angle orientations (LBFS-CA). In the present study, for each hole geometry, one row of 21 holes is employed with 3.5d spanwise spacing at a location 3.73 cm or 0.49c from the airfoil leading edge. The entrance diameter and length to entrance diameter ratio of all three types of holes are the same, 0.680 mm and 5.5, respectively. Table 1 gives the injectant flow conditions for all three film hole configurations. For each film hole geometry, the injectant Reynolds number, based on hole inlet average velocity and inlet hole diameter, then ranges from about 4×10^3 to about 2.6×10^4.

The present test section is useful and advantageous over cascade arrangements with multiple airfoils and significant flow turning because 1) the test section produces Mach numbers, nondimensional pressure variations, Reynolds numbers, passage mass flow rates, and physical dimensions that match values along airfoils in operating engines; 2) the airfoil provides the same suction surface boundary-layer development (in the same pressure gradient without flow turning) as exists in operating engines; 3) film cooling performance data are obtained on airfoil surfaces without the complicating influences of vortices present near airfoil leading edges, in the blade passages, and along airfoil pressure surfaces[23]; 4) results obtained with the arrangement are not configuration dependent; 5) only one airfoil is needed to obtain representative flow characteristics; and 6) most of the airfoil surface is accessible to infrared thermography for optical, surface temperature measurement. Thus, the present experiment is

Table 1 Experimental conditions

Hole geometry	m	ρ_c/ρ_m	p_{tc}/p_m	U_c/U_m	I	M_c/M_m
CYSA	0.46	1.29	1.14	0.17	0.36	0.41
CYSA	0.56	1.39	1.19	0.22	0.40	0.47
CYSA	0.69	1.44	1.29	0.33	0.48	0.57
CYSA	0.81	1.48	1.40	0.44	0.55	0.66
CYSA	1.02	1.55	1.64	0.66	0.65	0.81
LBFS-SA	0.41	1.25	1.10	0.14	0.33	0.35
LBFS-SA	0.57	1.47	1.19	0.22	0.39	0.47
LBFS-SA	0.68	1.48	1.26	0.31	0.46	0.55
LBFS-SA	0.75	1.44	1.37	0.39	0.52	0.64
LBFS-SA	1.02	1.49	1.72	0.69	0.68	0.86
LBFS-CA	0.43	1.27	1.11	0.15	0.34	0.36
LBFS-CA	0.49	1.36	1.15	0.18	0.36	0.42
LBFS-CA	0.59	1.48	1.20	0.24	0.40	0.48
LBFS-CA	0.69	1.54	1.27	0.31	0.45	0.56
LBFS-CA	0.80	1.51	1.38	0.42	0.53	0.65
LBFS-CA	0.86	1.56	1.46	0.47	0.55	0.71
LBFS-CA	1.01	1.53	1.65	0.67	0.66	0.82

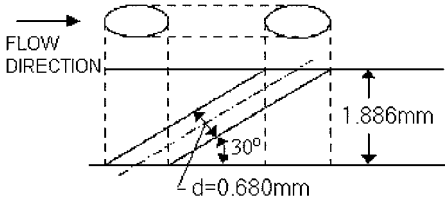

a) CYSA holes

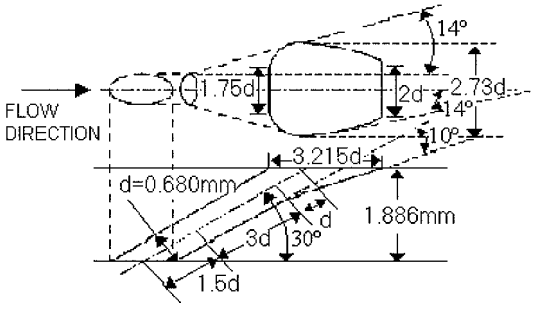

b) LBFS-SA holes

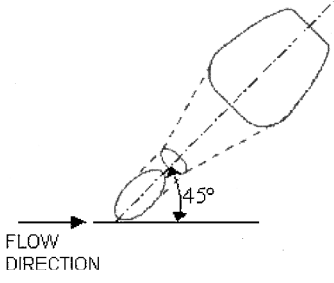

c) LBFS-CA holes

Fig. 2 Film cooling hole geometries.

designed to investigate suction surface film cooling from shaped holes with and without compound angle orientations, while matching Reynolds numbers, Mach numbers, pressure gradients, passage flow rates, boundary-layer development, and physical dimensions of airfoils in operating engines.

III. Experimental Apparatus and Procedures

A. Transonic Wind Tunnel

A schematic diagram of the Transonic Wind Tunnel (TWT) is shown in Fig. 3. The blowdown-type facility consists of two main parts: 1) compressor and storage tanks and 2) wind tunnel. The wind tunnel consists of five major subsections: 1) flow rate and pressure level management apparatus; 2) plenum tank; 3) inlet ducting and test section; 4) plenum, exit ducting, and ejector; and 5) control

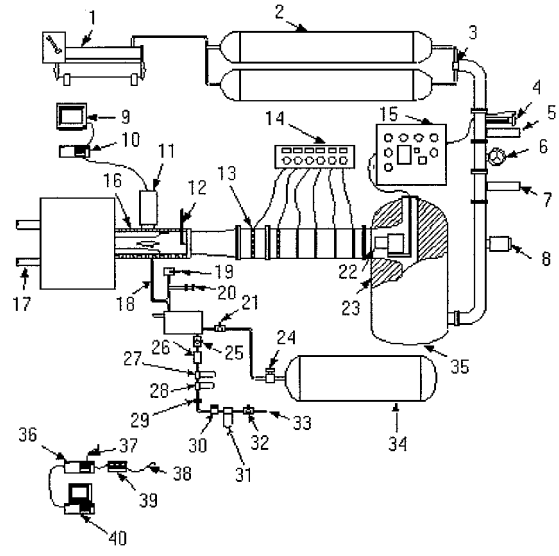

1. Compressor
2. Storage Tanks
3. Octopus Collection Manifold
4. Pressure Regulator
5. Pressure Relief Valve
6. Manual Valve
7. Pressure Relief Valve
8. Mass Flow Valve
9. Monitor
10. VCR
11. IR Camera
12. Pitot Tube
13. Resistance Strip Heaters
14. Strip Heater Control Panel
15. Flow/Internal Heater Control Panel
16. Test Section
17. Outlet Piping
18. Insulated Hose
19. Manual Valve
20. Automatic Valve
21. Manual Valve
22. Resistance Heater
23. Fire Brick
24. Manual Valve
25. Manual Valve
26. Rotameter
27. Dessicant Air Dryer
28. Coalescing Filter
29. Sonic Orifice Plate
30. Pressure Regulator
31. Particulate Filter
32. Manual Valve
33. Compressed Air Supply
34. Liquid Nitrogen Tank
35. Heater Tank
36. Data Acquisition Unit
37. Thermocouple Wires
38. Air Tubing
39. Pressure Transducers
40. Computer

Fig. 3 TWT including film injection system.

panel.[24] A Gardner Denver Company model RL-1155-CB compressor is used to pressurize the array of eight tanks, whose total capacity volume is 11.9 m^3. A VanAir VAS93039 model D16-5 Deliquescent desiccant dryer, a Pall Corporation 5EHG-4882-207 oil filter, and two Permanent Filter Corporation 13846 particulate filters are located just downstream of the compressor to remove particulates and moisture from the air. A Fisher pressure regulator with a 6X4 EWT design sliding gate valve, a Fisher-type 667 diaphragm actuator, a 3582 series valve positioner, and a Powers 535 one-quarter DIN process controller are used to regulate the pressure in the test section as the storage tanks discharge. A plenum tank, a 30.48-cm-i.d. pipe, a circular-to-square transition duct, a nozzle, and the test section then follow.

The freestream turbulence intensity at the test section inlet is measured with a single-wire hot-wire probe to be about 0.5%. As mentioned, the data presented at this low value of freestream turbulence intensity are valuable for design and for the development of numerical prediction schemes. Transonic data at such conditions are also valuable because they must be in hand before measurements at higher freestream turbulence intensity levels are understood. Relative humidity at the test section inlet is typically 20–30%. In spite of these values, no significant condensation of vapor is present near the film cooling hole exits. The test section is connected to a large $92.71 \times 91.44 \times 91.44$ cm plenum with square plastic and rubber flanges at its inlet. The plenum diffuses high-speed air from the test section exit into a reservoir of low-velocity air. This plenum is then connected to two ducts that are subsequently connected to the atmosphere.

B. Secondary Air Injection System and Mainstream Air Heating

The injection system is also shown in Fig. 3. From the building air supply, the air used for film cooling first enters a Norman Filters 5-μm ABS particulate filter, a Fairchild 10282 pressure regulator, a sonic orifice, a Wilkerson M16-02 F00B E95 coalescing filter, a Wilkerson X03-02-000AJ96 Desiccant dryer, a Dwyer Model RMC series rotameter, and a pressure relief valve. For every experimental test condition, the injectant mass flow rate measured with the sonic orifice is in excellent agreement with the flow rate measured with the rotameter. The dryers and filters are required to avoid frost buildup because a Xchanger Inc. TV-050 heat exchanger uses liquid nitrogen to cool injectant air to temperatures as low as -120°C. Also employed to heat the mainstream flow is a Leister model 8D8A type 10,000 "S" electrical heater. With this arrangement, ratios of coolant to freestream density ρ_c/ρ_m from 1.4 to 1.6 are easily achieved. The film injectant experimental conditions are given in Table 1, as mentioned.

C. Pressure and Temperature Measurements

As tests are conducted, Validyne Model DP15-46 pressure transducers (with diaphragms rated at either 345 or 1380 kPa) and calibrated copper–constantan thermocouples are used to sense pressures and temperatures at different locations throughout the facility. Signals from the transducers are processed by Celesco Model CD10D carrier demodulators. All pressure transducer measurement circuits are calibrated using a Wallace and Tiernan FA145 bourdon tube pressure gauge as a standard. A United Sensor PLC-8-KL pitot-static probe with an attached copper–constantan thermocouple is used to sense total pressure, static pressure, and recovery temperature at the inlet of the test section during each blowdown. From these data, the Mach number, total temperature, and static temperature are determined at the inlet of the test section.

D. Local Adiabatic Film Cooling Effectiveness Measurement

Coolant stagnation temperature is determined from measurement of the coolant recovery temperature just upstream of the coolant plenum using a calibrated copper–constantan thermocouple. With knowledge of the Mach number in this passage, the coolant stagnation temperature is then determined, after the measured temperature is corrected for time lag errors due to the finite size of the thermocouple junction. All adiabatic effectiveness experiments are repeated twice to verify the consistency and repeatability of the results.

Spatially resolved temperature distributions along the airfoil surface are determined using infrared imaging in conjunction with thermocouples, energy balances, digital image processing, and in situ calibration procedures. To accomplish this, the infrared radiation emitted by the Lexan surface of the airfoil is captured using a VideoTherm 340 Infrared Imaging Camera, which operates at infrared wavelengths from 8 to 14 μm. Temperatures, measured using calibrated, copper–constantan thermocouples distributed along the Lexan surface adjacent to the flow, are used to perform the in situ calibrations simultaneously as the radiation contours from surface temperature variations are recorded.

This is accomplished as the camera views the test surface through a custom-made, cylindrical zinc–selenide window (which transmits infrared wavelengths between 6 and 17 μm). This is installed just above the airfoil in the top contoured wall of the test section. Reflection and radiation from surrounding laboratory sources are minimized using an opaque shield that covers the camera lens and the zinc–selenide window. Three to four thermocouple junction locations are present in any field viewed by the camera. The exact spatial locations and pixel locations of these thermocouple junctions and the coordinates of a 5 × 5 cm field of view are known from calibration maps obtained before measurements. During this procedure, the camera is focused and rigidly mounted and oriented relative to the test surface in the same way as when radiation contours are recorded. With these data, gray scale values at pixel locations within video taped images from the infrared imaging camera are readily converted to temperatures. Because such calibration data depend strongly on camera adjustment, the same brightness, contrast, and aperture camera settings are used to obtain the experimental data. The in situ calibration approach rigorously and accurately accounts for these variations.[25]

Images from the infrared camera are recorded as 8-bit gray scale images on commercial videotape using a Panasonic AG-1960 video recorder. Images are then digitized using NIH Image version 1.60 software, operated on a Power Macintosh 7500 computer. This is done about 12.0 s after each blowdown begins because the film and freestream flows are established and to obtain data when the test surface approximates an adiabatic surface condition. Subsequently, software is used to determine coordinate locations along the target surface. This software also converts each of 256 possible gray scale values to temperature at each pixel location using calibration data and then determines values of local adiabatic film cooling effectiveness. Contour plots of local surface temperature and surface effectiveness are prepared using DeltaGraph version 4.0 software. Each individual image covers a 300 × 300 pixel area. Additional details on infrared imaging procedures are provided by Sargent et al.[25]

E. Data Acquisition System

Voltages from the carrier demodulators and thermocouples are read sequentially using Hewlett–Packard HP44222T and HP44222A relay multiplexer card assemblies, installed in a Hewlett–Packard HP3497A low-speed data acquisition/control unit. This system provides thermocouple compensation electronically such that voltages for type T thermocouples are given relative to 0°C. A Hewlett–Packard HP362 series computer processes signals from all transducers and thermocouples to give pressure and temperature readings, as well as other flow parameters.

F. TWT Qualifying Characteristics

At the inlet of the test section, the total pressure and static pressure show excellent spatial uniformity.[24] Total pressure and static pressure values vary by less than 1.38 kPa (or 0.7% of p_{tm}) as measurements are made at nine different probe locations. Mach numbers determined from these data then vary by less than 0.002. Steady conditions are maintained in the test section for 45-s-long time intervals.[24] Such characteristics are not only due to the TWT design, but also to the excellent performance characteristics of the TWT pressure regulator and its controller.

G. Experimental Uncertainties

Uncertainty estimates are based on 95% confidence levels and determined using procedures described by Kline and McClintock[26] and Moffat.[27] Mach number uncertainty is $\pm.002$. Uncertainty of temperatures is ±0.15°C. Pressure uncertainty is ±0.25 kPa. Discharge coefficient C_D uncertainty is $\pm.035$, for a typical nominal value of $C_D = 0.80$. Spatial and temperature resolutions achieved with the infrared imaging are about 0.05 mm and 0.8°C, respectively. This magnitude of temperature resolution is due to uncertainty in determining the exact locations of thermocouples with respect to pixel values used for the in situ calibrations. Local adiabatic film effectiveness uncertainty is then about ±0.015, or about $\pm6.0\%$, for a nominal effectiveness value of 0.25. These local effectiveness uncertainty values are slightly higher within about $1.0d$ of the hole exits due to some three-dimensional effects within the polycarbonate in the vicinity of the holes.

IV. Experimental Results

A. Test Section Flow Characteristics

The airfoil Mach number distribution is measured using a symmetric airfoil with 11 pressure taps located along the midspan line of the airfoil at various positions along its length. Eight of these taps lie on the top surface of the airfoil, and three taps are located on the bottom surface of the airfoil. Figure 4 shows measured Mach numbers along the airfoil surface, which range from about 0.4 to 1.14. Trailing-edge shock wave angles and total pressure changes indicate that the experimental Mach number at the airfoil trailing edge is about 1.24. Figure 4 also shows that values from both sides of the airfoil are in agreement. From these data, the mainstream

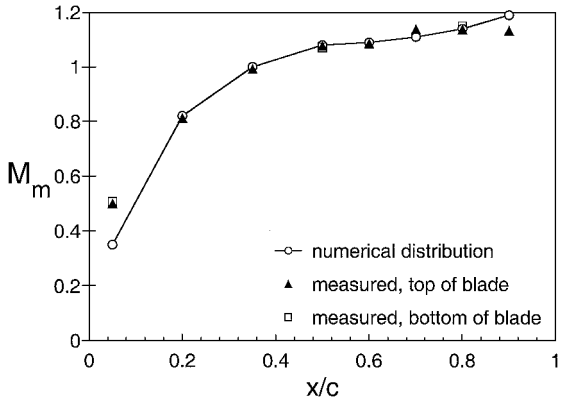

Fig. 4 Freestream Mach number distribution around the test airfoil; here, x is measured from the airfoil leading edge.

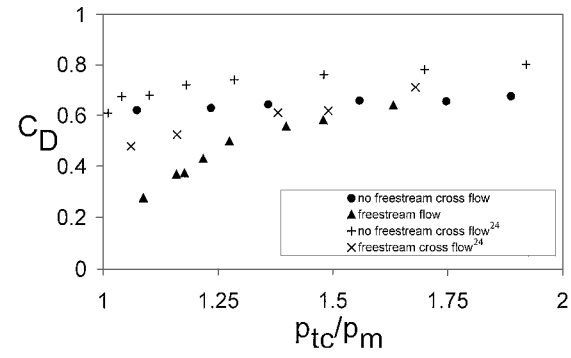

Fig. 5 Discharge coefficients, both with and without freestream crossflow, as dependent on coolant-to-freestream pressure ratio for CYSA holes, including comparisons with data from Jackson et al.[24]

Reynolds number, based on blade chord and flow conditions near the airfoil leading edge, is about 1.0×10^6.

Schlieren images presented by Jackson et al.[24] show a pair of trailing-edge oblique shock waves when flow is passing through the test section. From these results, it is evident that 1) the only shock waves present in the test section (with no film cooling) are a pair at the trailing edge of the symmetric airfoil, and these do not reflect off of the top and bottom walls of the test section and 2) the trailing-edge shock waves remain stationary and in place for the entire test sequence. The angle produced by the strong oblique shock waves at the airfoil trailing edge is about 73 deg (measured from the airfoil symmetry plane). This value and measured total pressures downstream of the oblique shock waves are in good agreement with theoretical values for a 5-deg flow deflection angle. The positions and shapes of these oblique shock waves also show good qualitative agreement with numerically computed, spatially resolved Mach number distributions, also presented by Jackson et al.[24] Note that this agreement and the agreement shown in Fig. 4 are present in spite of the fact that these two-dimensional numerical predictions, which are used to design the test section do not account for the boundary layers on the side walls of the test section.

B. Discharge Coefficients

Discharge coefficients are determined using

$$C_D = \dot{m}/\dot{m}_{\text{ideal}} \tag{1}$$

where the ideal mass flow rate is given by

$$\frac{\dot{m}_{\text{ideal}}}{A} = \sqrt{\frac{k}{R}}\frac{P_{tc}}{\sqrt{T_{tc}}}\left(\frac{M_c}{\left\{1+[(k-1)/2]M_c^2\right\}^{(k+1)/2(k-1)}}\right) \tag{2}$$

Here, A is the total cross-sectional area of the holes at their round inlets and M_c is the isentropic Mach number of the injectant at the exits of the film cooling holes. This Mach number is determined using the isentropic relation based on the ratio of the stagnation pressure in the injection plenum p_{tc} and the static pressure at the exits of the film cooling holes p_m.

Discharge coefficients for the CYSA holes from the present study are compared to ones from Jackson et al.[24] in Fig. 5. Jackson et al.[24] employ the same plenum arrangement as in the present study, except that the step on the plenum wall just in front of the film hole entrances (shown in Fig. 1b for the present configuration) is not present. In both cases, the hole exits are located on the suction surface of a turbine airfoil, where the freestream Mach number is nominally 1.07. In addition, the injectant enters the plenum from one side, and the other side of the plenum is closed for both investigations, as shown in Fig. 1c. For the comparison data,[24] a row of 21 holes is employed with length-to-entrance diameter ratio of 2.26, 4 d spanwise spacing, and an inclination angle of 35 deg. In the present study, the same number of holes are employed with length-to-entrance diameter ratio of 5.5, 3.5d spanwise spacing, and an inclination angle of 30 deg.

Figure 5 shows that the present C_D data are lower than the Ref. 24 data when compared at the same pressure ratio, regardless of whether or not freestream crossflow is present. These differences are mostly due to the effects of the step (located just in front of the hole entrances) in the plenum, which is used in the present study, but not in the investigation by Jackson et al.[24] The C_D differences are due in only small part to the different CYSA film hole geometries employed in the two studies. With no freestream crossflow present, the step then results in two different phenomena:

1) There is a small region of separated, recirculating flow just outside of the holes near their entrances.

2) The step acts to funnel the plenum flow near the hole entrances so that injectant velocities near these locations are significantly higher than if no step is present.

These higher approach velocities result in a larger region of recirculating, separated flow, which is present within the entrance region of each film hole. This enlarged separated flow zone and the increased velocities as the flow turns (relative to the hole axis) then give greater losses of total pressure. This leads to lower discharge coefficients for the present configuration (with the step) as the flow advects through the holes.

Both the present C_D data and the C_D data from Jackson et al.,[24] measured for CYSA holes with freestream crossflow, are lower than data measured with no freestream crossflow in Fig. 5. Freestream crossflows often result in reduced discharge coefficients.[28] However, the reductions observed in Fig. 5 are greater than those expected when a plenum condition with zero Mach number is employed near the hole entrances and a freestream with finite Mach number is present at the hole exits. This is because a true plenum condition does not exist at the hole entrances in the present study, as mentioned. Instead, the nonuniform variation of injectant velocity from local jetting near the hole entrances gives local Mach numbers as high as about 0.5 at the highest blowing ratios investigated.

According to Hay et al.,[28,29] discharge coefficients decrease (at particular values of the p_{tc}/p_m pressure ratio) either as the injectant crossflow Mach number increases, or as the angle between the injectant direction and the freestream direction becomes larger. This is consistent with C_D results from the present investigation with freestream crossflow. Note that the present overall plenum geometry (with flow entering only from one side) induces flow that is perpendicular to the mainstream direction. However, the addition of the step, located in the plenum just upstream of the hole entrances (mentioned earlier), intensifies this effect when freestream crossflow is also present. This is because the step causes the injectant to be locally accelerated and further constrained (or funneled) in a direction perpendicular to the external freestream flow. As a result, pressure losses are augmented as the injectant flow first turns to enter the holes, passes through the holes, then turns again as it exits the holes, and encounters the mainstream crossflow. This then gives more pronounced separation zones compared to the arrangement employed by Jackson et al.[24] As a result, compared to the Jackson

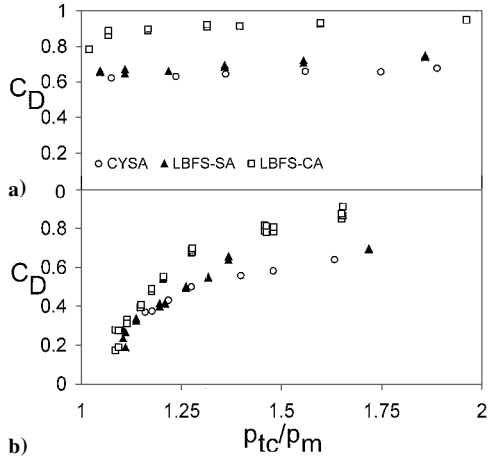

Fig. 6 Discharge coefficients as dependent on coolant-to-freestream pressure ratio for CYSA, LBFS-SA, and LBFS-CA holes: a) with no freestream crossflow and b) with freestream crossflow.

et al. data, total pressure losses are greater, and C_D decreases are larger on a percentage basis relative to the data measured with no freestream crossflow.

Discharge coefficients, measured at different injectant to freestream pressure ratios, are presented without and with freestream external flow in Figs. 6a and 6b, respectively. Data are given for all three hole configurations, CYSA, LBFS-SA, and LBFS-CA. Comparing Figs. 6a and 6b reveals that C_D data with freestream crossflow approach the data with no freestream crossflow as p_{tc}/p_m increases (for each of these hole geometries). Thus, the influences of freestream crossflow on discharge coefficients are reduced at higher pressure ratios as the overall level of injectant momentum increases, an observation also made in other investigations.[24,28–30]

With or without freestream external flow, Figs. 6a and 6b also show that the LBFS-CA discharge coefficient data are higher (when compared at the same pressure ratio) than the CYSA data and LBFS-SA data at most values of p_{tc}/p_m examined. The LBFS-SA data are then slightly higher than the CYSA data for all p_{tc}/p_m in Fig. 6a (when no freestream crossflow is present), and for $p_{tc}/p_m > 1.3$ in Fig. 6b (with freestream crossflow). Such behavior means that the most important effect influencing these C_D magnitudes is the internal injectant crossflow condition. The flared hole shaping normally increases discharge coefficient values because of its action in diffusing the injectant flow and increasing pressure recovery. According to Figs. 6a and 6b, this effect is largest when freestream crossflow is present and $p_{tc}/p_m > 1.3$. However, because the cylindrical section before the flare (for the LBFS holes) is less than two hole diameters in length, there is not adequate room for the injectant flow to reattach before it reaches the flared portion of the holes. This then reduces the diffusing action of the flared geometry[30] and results in smaller discharge coefficient increases relative to CYSA holes.

The present LBFS-CA discharge coefficient data are then higher than the LBFS-SA data because more turning of the flow is required in the latter case as the injectant enters the holes. The coolant crossflow and the hole axis are oriented perpendicular to each other with LBFS-SA holes, which means that no velocity component of the internal crossflow exists in the direction of the hole axis, and the coolant must turn 90 deg to enter the hole. Figures 6a and 6b illustrate this behavior regardless of whether or not freestream crossflow is present. Such large changes with the internal crossflow conditions are tied to the existence, size, and location of a separated region at the entrance of each film cooling hole. This separation zone, which is the present at the upstream edge of each hole, increases in size as the angle between the hole axis and the approaching injectant increases. This then gives increased pressure losses and lower C_D magnitudes for LBFS-SA holes compared to LBFS-CA holes. In addition, with freestream crossflow (Fig. 6b), increasing angle of orientation means that higher p_{tc}/p_m values are needed before discharge coefficients flatten out into a plateau region.[29]

Note that, in contrast to results described by Hay et al.,[29] Hay and Lampard,[30] and others, M_m and p_m are held constant at the hole exits in the present investigation as the coolant mass flow rate is changed. Consequently, as p_{tc}/p_m is varied with the present plenum arrangement, the injectant Mach number in the plenum near the hole entrances and M_c (the isentropic Mach number at the hole exits) both change (see Table 1). This is then similar to the injectant behavior in operating turbine airfoils, where the injectant crossflow Mach number and the p_{tc}/p_m pressure ratio can not be varied independently of each other.

C. Local Adiabatic Film Cooling Effectiveness Distributions

Because the present measurements are made in a transonic environment, the local adiabatic film cooling effectiveness is determined using an equation of the form

$$\eta = \frac{(T_{\text{aw}} - T_{rm})}{(T_{tc} - T_{rm})} \tag{3}$$

Here, T_{rm} is the freestream recovery temperature at the location of the film cooling holes. This is determined from test section inlet stagnation temperature, the recovery factor for turbulent boundary layers, and the local freestream Mach number at the location of the film cooling holes. The temperature T_{tc} in Eq. (3) is the coolant stagnation temperature.

Distributions of the local, surface adiabatic film cooling effectiveness for LBFS-CA, LBFS-SA, and CYSA hole geometries are presented in Figs. 7a–7c for ρ_c/ρ_m of 1.44–1.51. These data are given for blowing ratios m of 0.81 for CYSA holes, 0.75 for LBFS-SA holes, and 0.80 for LBFS-CA holes. In all three cases, the effectiveness data are given as dependent on normalized spanwise distance z/d and normalized streamwise distance x/d . Freestream flow direction is from top to bottom in each image, and the downstream edge of the film cooling holes are located at $x/d = 0$. Darker regions in each image represent areas of lower adiabatic surface temperature and higher local adiabatic film cooling effectiveness. The uneven nature of the contours in each plot results from the limited resolution of the camera in resolving surface temperatures over very small distances (because the holes are so small relative to the distance to the camera, which must be located outside of the test section) and because each effectiveness distribution is determined from an instantaneous infrared image.

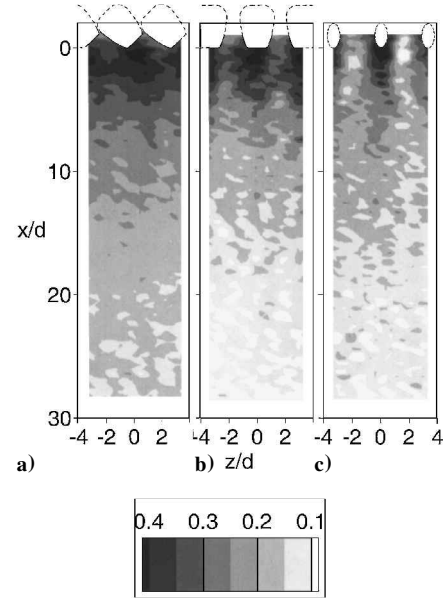

Fig. 7 Local, surface adiabatic film cooling effectiveness distributions for $m = 0.75$–0.81 and $\rho_c/\rho_\infty = 1.44$–$1.51$: a) LBFS-CA, b) LBFS-SA, and c) CYSA holes.

The CYSA data in Fig. 7c show high local values of adiabatic effectiveness just downstream of each film cooling hole. However, relative to the size of each hole, each of these highly augmented effectiveness regions is quite small and is contained within a strip of higher effectiveness that extends in the streamwise direction downstream of each hole. Note that these higher surface effectiveness distributions are slightly skewed to one side of each hole at x/d from 0 to 5 because the injectant approaches each hole entrance in a cross stream direction. Such high effectiveness regions are limited in spatial extent because of the liftoff of the largest film concentrations from the test surface as it emerges from each CYSA injection hole. Lower effectiveness values between 0.1 and 0.2 are then found between the film cooling holes near $x/d = 0$. As the injectant becomes more diffuse, effectiveness values are then more uniform across the span of the test surface, ranging from 0.12 to 0.25 near $x/d = 10$.

Regions with high values of adiabatic film cooling effectiveness are spread over much larger portions of the test surface downstream of the LBFS-SA holes in Fig. 7b. Here, regions with effectiveness magnitudes greater than 0.35 are about the same size as the exit areas of these laid-back-fan-shaped holes. Effectiveness magnitudes between 0.2 and 0.3 are then present between the film cooling holes near $x/d = 0$. Values then range from 0.12 to 0.25 near $x/d = 10$. Even though the diffusing action of the flared hole geometry is reduced somewhat because the cylindrical section before the flare is less than two hole diameters in length (as mentioned), Fig. 7b shows that the shaping employed still leads to improvements in surface effectiveness distributions. This is due to the action of these holes in lowering the injectant momentum at the hole exits and in spreading more injectant closer to the test surface and over larger spanwise surface areas as it exits the holes. As for the CYSA holes, Fig. 7b indicates that the injectant from LBFS-SA holes is skewed to one side of each hole because the injectant crossflow is perpendicular to the hole axis.

Figure 7a then shows that additional benefits in protection result when the shaped holes are arranged with compound angle orientations. This is because the compound angles give increased lateral spreading and greater injectant concentrations near the surface,[14,31] which gives important benefits when employed in combination with shaping, which gives less jet penetration, lower velocity gradients, and more flow diffusion.[14] The overall result is more spanwise uniform spreading of the largest injectant concentrations along the test surface just downstream of the holes. Effectiveness magnitudes then range between 0.3 and 0.4 between the film cooling holes near $x/d = 0$, and between 0.15 to 0.25 near $x/d = 10$. The highest effectiveness values are then about the same as for the LBFS-SA holes. LBFS-CA improvements relative to the LBFS-SA holes are then a result of more uniform effectiveness distributions around and just downstream of the compound angle oriented holes.

D. Spanwise-Averaged Adiabatic Effectiveness Distributions

Spanwise-averaged adiabatic effectiveness are determined by averaging local adiabatic effectiveness distributions, such as the ones in Figs. 7a–7c from $z/d = -17.74$ to $+17.74$, which covers the middle 10 holes in each infrared image. Spanwise-averaged adiabatic effectiveness data for the CYSA holes, LBFS-SA holes, and LBFS-CA holes are given in Figs. 8a–8c, respectively. Perpendicular injection data from Gritsch et al.[17] are included in Figs. 8a and 8b for comparison. Data from Bell et al.[14] are given in Fig. 8a for comparison and show agreement with the present data for a blowing ratio of about 0.7.

In Fig. 8a, the lowest spanwise-averaged effectiveness distribution for CYSA holes is present for a blowing ratio m of 0.46. The highest spanwise-averaged effectiveness distribution is then measured at a blowing ratio of 1.02. In between, spanwise-averaged adiabatic effectiveness values become higher as the blowing ratio increases and lower as streamwise distance increases. This trend with blowing ratio is different from some other CYSA data,[14] in which an injectant plenum condition is employed or the injectant approaches the holes parallel to the hole axis. However, the observed trend is consistent with data from Ref. 17 for $x/d > 2$, wherein the

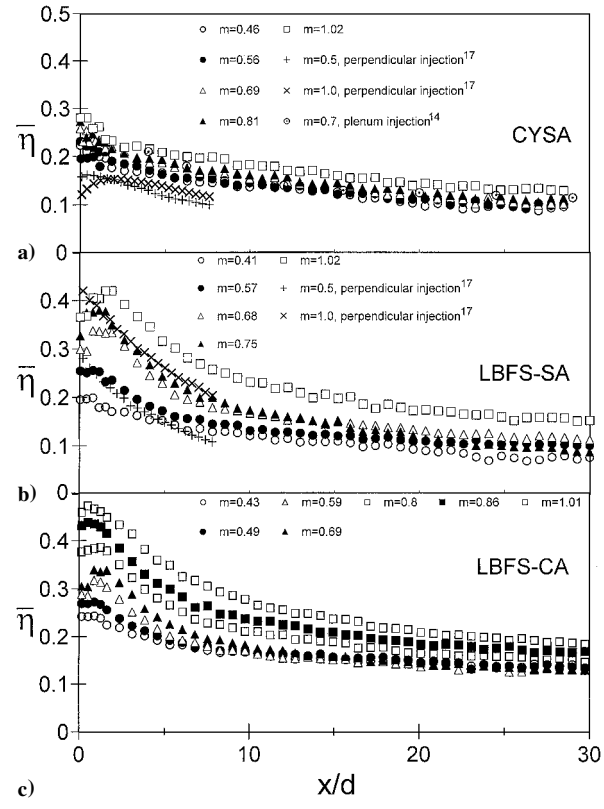

Fig. 8 Spanwise-averaged, surface adiabatic film cooling effectiveness distributions: a) CYSA, b) LBFS-SA, and c) LBFS-CA holes.

injectant approaches the hole entrances with a coolant Mach number of 0.6 in a direction that is perpendicular to the hole axis.

Note that the effectiveness data from the present study are higher than the ones reported by Gritsch et al.[17] in Fig. 8a for a number of reasons. Most important, a row of holes is employed in the present study, which causes larger film concentrations to interact with each other, and to remain nearer the surface, than when a single hole is employed, as is done in the Gritsch experiment. Another important difference between the present data and those from Ref. 17 relates to the freestream conditions. The data from the latter study are obtained with a constant freestream Mach number of 0.6, and no shock waves develop in the vicinity of the hole exits. Here, the local Mach number at the locations of the holes is nominally 1.07, which results in one or more oblique shock waves just upstream of or in the immediate vicinity of the holes.[32] According to Ligrani et al.,[32] with perpendicular film injection at the hole entrances (as employed here), the addition of shock waves act to decrease magnitudes of local and spanwise-averaged effectiveness (compared to flows with no shock waves). Thus, the differences between the present data and the Gritsch et al.[17] data would be even larger if the present data are obtained at their constant freestream Mach number of 0.6. Other differences in the plenum arrangements and flow conditions employed in the two studies may result in some additional $\bar{\eta}$ differences. However, these are smaller than those due to hole number and shock wave effects. Note that the Gritsch et al.[17] data are chosen for comparison because this is the only other known study that considers LBFS holes at higher Mach numbers in the vicinity of 1.0.

The LBFS-SA hole data in Fig. 8b also show increasing $\bar{\eta}$ values at each x/d location as m increases from 0.41 to 1.02. Notice that the locations of maximum spanwise-averaged effectiveness shift from $x/d = 1.0$ to 3.0 as the blowing ratio increases from 0.41 to 1.02. Spanwise-averaged effectiveness values at each blowing ratio then decrease with increasing x/d downstream of these local $\bar{\eta}$ maxima. Such trends are consistent with LBFS-SA hole configuration data reported by Gritsch et al.[17] for a perpendicular injection plenum condition. Notice that the $m = 0.5$ LBFS-SA data from Ref. 17 (obtained with a $M_m = 0.6$ and a coolant crossflow Mach number of 0.6)

are just slightly lower than the present data for $m = 0.57$ in Fig. 8b. When $m = 1.02$, the present data show the same trend as the Gritsch $m = 1.0$ data, but they are about 0.5 effectiveness units higher. As mentioned, such differences are mostly due to the different number of holes employed across the test surface in the two studies, that is, 1 and 21. This illustrates that experimental conditions and configuration geometries are rarely matched precisely when different film cooling studies are compared to each other. Different geometries, test configurations, and flow conditions give different results, which means that comparisons are not likely the same when any of these parameters is changed. Here, the film cooling hole configurations investigated are unique because they are considered in transonic flows with oblique shock waves, a favorable pressure gradient, and suction surface geometry and boundary-layer development that match those in operating engines. No other investigation known to the present authors addresses the behavior of shaped, compound angle hole configurations under such conditions.

The LBFS-CA spanwise-averaged effectiveness data in Fig. 8c also increase with blowing ratio m at each x/d location, where m ranges from 0.43 to 1.01. The locations of the maximum spanwise-averaged effectiveness are located around $x/d = 1.5$ for each blowing ratio considered in this range. Effectiveness values then become lower (for each m value) as the streamwise distance increases downstream of these $\bar{\eta}$ maxima.

Spanwise-averaged adiabatic effectiveness values for all three hole geometries (CYSA, LBFS-SA, and LBFS-CA) are compared to each other at fixed blowing ratios in Figs. 9a–9c. Data are given for m of 0.68–0.69 in Fig. 9a, 0.75–0.81 in Fig. 9b, and 1.01–1.02 in Fig. 9c. In Fig. 9c (at the highest blowing ratio of 1.01–1.02), spanwise-averaged effectiveness values measured downstream of the LBFS-CA holes are higher than the data measured downstream of the CYSA holes and the LBFS-SA holes when compared at the same x/d. The LBFS-SA data then lie between the CYSA data and the LBFS-CA data. This is because the momentum of the LBFS-SA film distributions are reduced by the expanded hole exits, which causes the jets to not penetrate as far into the main flow and to stay closer to the surface at farther downstream locations compared to the CYSA produced films. Spanwise-averaged effectiveness values for LBFS-CA holes are higher than the ones for LBFS-SA holes because of increased lateral spreading and greater injectant concentrations near the surface over longer streamwise distances.

Somewhat different trends are evident in Fig. 9b for $m = 0.75$–0.81. Here, at smaller $x/d < 2$, the spanwise-averaged LBFS-SA data are in agreement with the spanwise-averaged LBFS-CA data. However, as these film cooling flows advect downstream, the advantages of the compound angles become apparent as the LBFS-CA data become significantly higher than the LBFS-SA data. This is a partial consequence of the interactions and film and mainstream momentum fields, as well as the different vortex structures that form on either side of the film concentrations from the two types of holes. Two vortices with about the same strengths, but opposite directions of rotation, form on either side of the film concentrations from the LBFS-SA holes. The upwash region between these two vortices then more readily advects film concentrations away from the test surface (giving lower spanwise-averaged $\bar{\eta}$ values) than when the two counter-rotating vortices, which are significantly different in size and strength, form around the LBFS-CA film concentrations.

The lower $\bar{\eta}$ values downstream of the CYSA holes, compared to those downstream of the LBFS-SA holes in Fig. 9b, are also strongly related to the momentum fields produced and the vortex pairs that form. Of particular importance are the strong, counter-rotating vortices that form on opposite sides of the CYSA produced film concentrations. Because of vortex induction and the small spanwise distance between the two vortices, the action of their secondary flow is particularly effective in advecting large film concentrations away from the test surface at small x/d (Ref. 33).

Such differences between $\bar{\eta}$ values downstream of the CYSA and LBFS-SA holes continue to persist at m of 0.68–0.69 in Fig. 9a. Here, LBFS-CA and LBFS-SA data show reasonable agreement at most all x/d values, with higher magnitudes than the ones measured downstream of the CYSA holes at $x/d < 8$–9.

The effects of blowing ratio on spanwise-averaged adiabatic effectiveness values are shown in Figs. 10a and 10b at $x/d = 1.0$ and 5.0, respectively. Note that values become higher for all three hole geometries as the blowing ratio increases. In Figs. 10a and 10b, spanwise-averaged adiabatic effectiveness values for LBFS-SA holes at both x/d are about the same as values for the CYSA holes at a blowing ratio of 0.41, but then become higher as the blowing ratio increases. Spanwise-averaged adiabatic effectiveness for LBFS-CA holes are then generally higher than the values produced by both the CYSA holes and the LBFS-SA holes for most of the m values considered. Such behavior illustrates the increases in protection that are provided by the LBFS-CA holes compared to LBFS-SA and CYSA configurations at small x/d , especially at higher blowing ratios near 1.0.

Similar conclusions are reached after inspection of the $\bar{\eta}$ data presented as dependent on momentum flux ratio I in Figs. 11a and

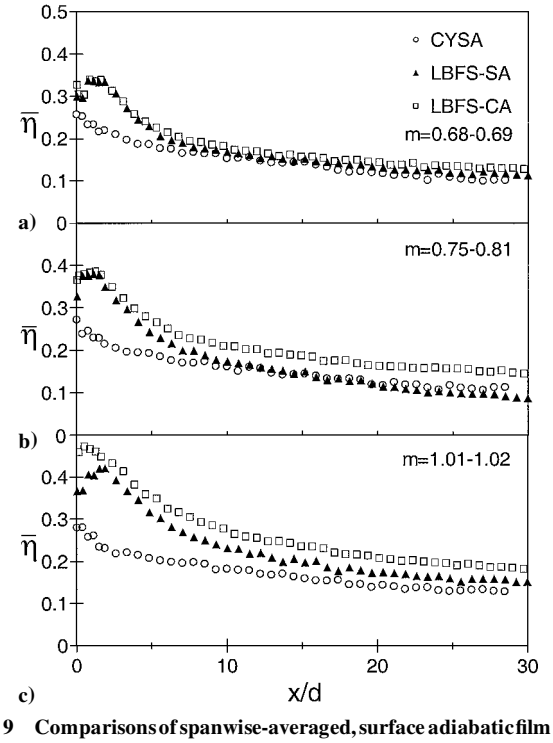

Fig. 9 Comparisons of spanwise-averaged, surface adiabatic film cooling effectiveness distributions for CYSA, LBFS-SA, and LBFS-CA holes: a) $m = 0.68$–0.69, b) $m = 0.75$–0.81, and c) $m = 1.01$–1.02.

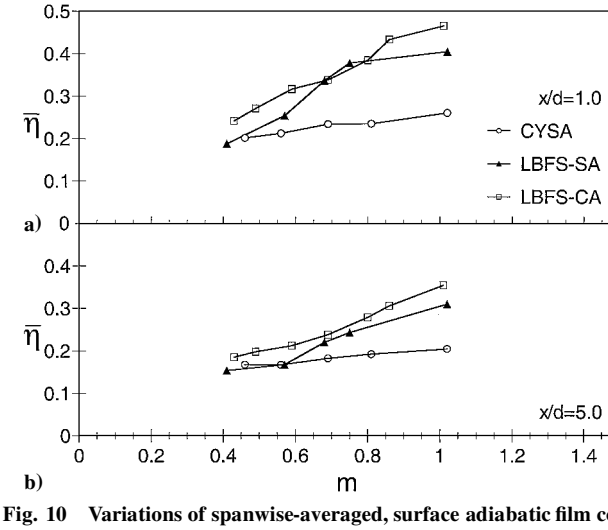

Fig. 10 Variations of spanwise-averaged, surface adiabatic film cooling effectiveness distributions for CYSA, LBFS-SA, and LBFS-CA holes with blowing ratio m: a) $x/d = 1.0$ and b) $x/d = 5.0$.

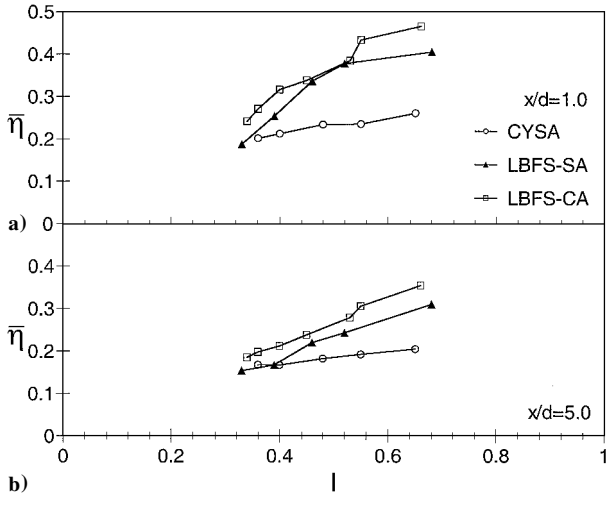

Fig. 11 Variations of spanwise-averaged, surface adiabatic film cooling effectiveness distributions for CYSA, LBFS-SA, and LBFS-CA holes with momentum flux ratio *I*: a) *x/d* = 1.0 and b) *x/d* = 5.0.

11b. Here, differences in spanwise-averaged effectiveness values between the three hole geometries become greater as I increases from about 0.3 to 0.7. Figures 10 and 11, thus, indicate that neither blowing ratio nor momentum flux ratio are adequate parameters, by themselves, for scaling spanwise-averaged effectiveness data produced by different shaped-hole configurations in transonic flow.

V. Summary

Film cooling adiabatic effectiveness distributions and discharge coefficients are presented for blowing ratios from 0.41 to 1.02, Mach number ratios from 0.3 to 0.9, coolant stagnation to freestream static pressure ratios from 1.1 to 1.7, and density ratios from 1.4 to 1.6. These are measured using a symmetric turbine airfoil with three different film cooling hole configurations located just downstream of the passage throat where the freestream Mach number is nominally 1.07: 1) CYSA, 2) LBFS-SA, and 3) LBFS-CA. The entrance diameter and length-to-entrance-diameter ratio of all three types of holes are the same, 0.680 mm and 5.5, respectively. The University of Utah TWT is employed for the tests. This blowdown facility provides excellent test section inlet uniformity, steady flow properties over time intervals as long as 45 s, and a Mach number distribution over the airfoil ranging from 0.4 to 1.24, which matches the distribution on the suction surfaces of airfoils from operating transonic, first turbine stages in gas turbine engines.

Local and spanwise-averaged surface adiabatic film cooling effectiveness distributions are measured using infrared imaging procedures. According to these data, the highest local and spanwise-averaged values of effectiveness, for the present experimental conditions and test section geometry, are produced using the combination of hole shaping and compound angles. The expanded hole exits from shaping result in reduced magnitudes of injectant momentum at the exits of the LBFS film holes. This gives lower velocity gradients, which causes the injectant not to penetrate as far into the main flow. The compound angles employed with the LBFS-CA holes give increased lateral spreading of the injectant, which causes the largest concentrations of the injectant to remain closer to the surface at locations farther downstream. This produces more spanwise uniform injectant and surface effectiveness distributions.

Note that discharge coefficients are also highest with LBFS-CA holes compared to the other two hole geometries considered. These data, as well as the effectiveness data, are strongly influenced by the injection plenum condition, the vortices that form around the injectant concentrations, as well as the shock waves that form near the hole exits in the transonic external flow environment. A plenum condition is not present upstream of the holes because the injectant approaches the hole entrances in a direction that is perpendicular to the hole axes with local jetting. Here, local crossflow Mach numbers may be as high as 0.5. A small step in the injection plenum is believed to accentuate this jetting effect. As a result, discharge coefficients for LBFS-CA holes are higher than ones from LBFS-SA holes because more flow turning is required at the entrances of the LBFS-SA holes.

Overall, these data illustrate the importance of obtaining film cooling data under conditions that simulate those in operating engines. Data obtained under subsonic conditions, or with slightly different experimental conditions or geometry, may not be accurate or applicable when complicated hole geometries are employed in high-speed, transonic, compressible flows with oblique shock waves, a favorable pressure gradient, suction surface geometry, and suction surface boundary-layer development.

Acknowledgment

This work was sponsored by the National Science Foundation Grant CTS-9615196.

References

[1]Goldstein, R. J., Eckert, E. R. G., and Burggraf, F., "Effects of Hole Geometry and Density on Three-Dimensional Film Cooling," *International Journal of Heat and Mass Transfer*, Vol. 17, 1974, pp. 595–607.

[2]Chen, P.-H., Ai, D., and Lee, S.-H., "Effects of Compound Angle Injection on Flat-Plate Film Cooling Through a Row of Conical Holes," American Society of Mechanical Engineers, ASME Paper 98-GT-459, 1998.

[3]Makki, Y. H., and Jakubowski, G. S., "Experimental Study of Film Cooling from Diffused Trapezoid Shaped Holes," AIAA Paper 86-1326, 1986.

[4]Ajersch, P., Zhou, J.-M., Ketler, S., Salcudean, M., and Gartshore, I. S., "Multiple Jets in a Crossflow: Detailed Measurements and Numerical Simulations," American Society of Mechanical Engineers, ASME Paper 95-GT-9, 1995.

[5]Farmer, J. P., Seager, D. J., and Liburdy, J. A., "The Effect of Shaping Inclined Slots on Film Cooling Effectiveness and Heat Transfer Coefficient," American Society of Mechanical Engineers, ASME Paper 97-GT-339, 1997.

[6]Schmidt, D. L., Sen, B., and Bogard, D. G., "Film Cooling with Compound Angle Holes: Adiabatic Effectiveness," *Journal of Turbomachinery*, Vol. 118, No. 4, 1996, pp. 807–813.

[7]Haven, B. A., and Kurosaka, M., "Effect of Hole Geometry on Liftoff Behavior of Coolant Jets," AIAA Paper 96-0618, 1996.

[8]Hyams, D. G., and Leylek, J. H., "A Detailed Analysis of Film Cooling Physics, Part III: Streamwise Injection with Shaped Holes," American Society of Mechanical Engineers, ASME Paper 97-GT-271, 1997.

[9]Brittingham, R. A., and Leylek, J. H., "A Detailed Analysis of Film Cooling Physics, Part IV: Compound-Angle Injection with Shaped Holes," American Society of Mechanical Engineers, ASME Paper 97-GT-272, 1997.

[10]McGrath, E. L., and Leylek, J. H., "Physics of Hot Crossflow Ingestion in Film Cooling," American Society of Mechanical Engineers, ASME Paper 98-GT-191, 1998.

[11]Berger, P. A., and Liburdy, J. A., "A Near-Field Investigation into the Effects of Geometry and Compound Angle on the Flowfield of a Row of Film Cooling Holes," American Society of Mechanical Engineers, ASME Paper 98-GT-279, 1998.

[12]Yu, Y., Yen, C.-H., Shih, T. I.-P., Chyu, M. K., and Gogineni, S., "Film Cooling Effectiveness and Heat Transfer Coefficient Distributions Around Diffusion Shaped Holes," American Society of Mechanical Engineers, ASME Paper 99-GT-34, 1999.

[13]Chen, P.-H., Ding, P.-P., Hung, M.-S., and Shih, P.-C., "Film Cooling over a Concave Surface Through a Row of Expanded Holes," American Society of Mechanical Engineers, ASME Paper 99-GT-33, 1999.

[14]Bell, C. M., Hamakawa, H., and Ligrani, P. M., "Film Cooling from Shaped Holes," *Journal of Heat Transfer*, Vol. 122, No. 2, 2000, pp. 224–232.

[15]Giebert, D., Gritsch, M., Schulz, A., and Wittig, S., "Film-Cooling from Holes with Expanded Exits: A Comparison of Computational Results with Experiments," American Society of Mechanical Engineers, ASME Paper 97-GT-163, 1997.

[16]Thole, K., Gritsch, M., Schulz, A., and Wittig, S., "Flowfield Measurements for Film-Cooling Holes with Expanded Exits," *Journal of Turbomachinery*, Vol. 120, No. 2, 1998, pp. 327–336.

[17]Gritsch, M., Schulz, A., and Wittig, S., "Adiabatic Wall Effectiveness Measurements of Film-Cooling Holes with Expanded Exits," *Journal of Turbomachinery*, Vol. 120, No. 3, 1998, pp. 549–556.

[18]Reiss, H., and Bolcs, A., "Experimental Study of Showerhead Cooling on a Cylinder Comparing Several Configurations Using Cylindrical and Shaped Holes," American Society of Mechanical Engineers, ASME Paper 99-GT-123, 1999.

[19]Teng, S., and Han, J. C., "Effect of Film-Hole Shape on Turbine Blade Heat Transfer Coefficient Distribution," AIAA Paper 2000-1035, 2000.

[20] Kohli, A., and Thole, K. A., "Entrance Effects on Diffused Film Cooling Holes," American Society of Mechanical Engineers, ASME Paper 98-GT-402, 1998.

[21] Khole, A., and Bogard, D. G., "Effects of Hole Shape on Film Cooling with Large Angle Injection," American Society of Mechanical Engineers, ASME Paper 99-GT-165, 1999.

[22] Cho, H. H., Rhee, D. H., and Kim, B. G., "Film Cooling Effectiveness and Heat/Mass Transfer Coefficient Measurement Around a Conical-Shaped Hole with a Compound Angle Injection," American Society of Mechanical Engineers, ASME Paper 99-GT-38, 1999.

[23] Brandt, H., Ganzert, W., and Fottner, L., "A Presentation of Detailed Experimental Data of a Suction Side Film Cooled Turbine Cascade," American Society of Mechanical Engineers, ASME Paper 2000-GT-296, 2000.

[24] Jackson, D. J., Lee, K. L., Ligrani, P. M., and Johnson, P. D., "Transonic Aerodynamic Losses Due to Turbine Airfoil, Suction Surface Film Cooling," *Journal of Turbomachinery*, Vol. 122, No. 2, 2000, pp. 317–326.

[25] Sargent, S. R., Hedlund, C. R., and Ligrani, P. M., "An Infrared Thermography Imaging System for Convective Heat Transfer Measurements in Complex Flows," *Measurement Science and Technology*, Vol. 9, No. 12, 1998, pp. 1974–1981.

[26] Kline, S. J., and McClintock, F. A., "Describing Uncertainties in Single Sample Experiments," *Mechanical Engineering*, Vol. 75, 1953, pp. 3–8.

[27] Moffat, R. J., "Describing the Uncertainties in Experimental Results," *Experimental Thermal and Fluid Science*, Vol. 1, No. 1, 1988, pp. 3–17.

[28] Hay, N., Lampard, D., and Benmansour, S., "Effect of Crossflows on the Discharge Coefficient of Film Cooling Holes," *Journal of Engineering for Power*, Vol. 105, No. 2, 1983, pp. 243–248.

[29] Hay, N., Henshall, S. E., and Manning, A., "Discharge Coefficient of Holes Angled to the Flow Direction," *Journal of Turbomachinery*, Vol. 115, No. 1, 1994, pp. 92–96.

[30] Hay, N., and Lampard, D., "The Discharge Coefficient of Flared Film Cooling Holes," American Society of Mechanical Engineers, ASME Paper 95-GT-15, 1995.

[31] Ligrani, P. M., Wigle, J. M., Ciriello, S., and Jackson, S. M., "Film Cooling from Holes with Compound Angle Orientations: Part 1—Results Downstream of Two Staggered Rows of Holes with 3d Spanwise Spacing," *Journal of Heat Transfer*, Vol. 116, No. 3, 1994, pp. 341–352.

[32] Ligrani, P. M., Saumweber, C., Schulz, A., and Wittig, S., "Shock Wave—Film Cooling Interactions in Transonic Flows," *Journal of Turbomachinery*, Vol. 123, No. 4, 2001, pp. 788–797.

[33] Haven, B. A., and Kurosaka, M., "Kidney and Anti-Kidney Vortices in Crossflow Jets," *Journal of Fluid Mechanics*, Vol. 352, 1997, pp. 27–64.